Roller-compaction-assisted binder jetting of textured ceramics

Mohammadamin Moghadasi[a], Josephine Jaraczewski[b], Alireza Mahdaviarab[c], Zhijian Pei[d], Chao Ma[a,d,e,f,*]

[a] Department of Materials Science and Engineering, Texas A&M University, College Station, TX, USA

[b] Department of Biomedical Engineering, Texas A&M University, College Station, TX, USA

[c] Department of Computer Science and Engineering, Texas A&M University, College Station, TX, USA

[d] Department of Industrial and Systems Engineering, Texas A&M University, College Station, TX, USA

[e] Department of Engineering Technology and Industrial Distribution, Texas A&M University, College Station, TX, USA

[f] School of Manufacturing Systems and Networks, Arizona State University, Mesa, AZ, USA

*Corresponding author. E-mail address: chao_ma@asu.edu (Chao Ma)

Abstract

Texturing is an approach to tailoring the properties of materials along the specific directions by arranging and growing grains directionally. In this work, a commercially available binder jetting machine equipped with the roller compaction feature was used to fabricate the textured ceramics via templated grain growth. Two types of powders were prepared: one with 100 wt.% alumina nanoparticles as the baseline, and the other with 75 wt.% alumina nanoparticles as the matrix and 25 wt.% alumina nanoplatelets as the templates for grain growth. The bulk density of the sintered samples with the alumina nanoplatelets was 4% lower than that without them. The scanning electron microscopy and X-ray diffraction results showed that morphological and crystallographic textures were achieved in the samples containing the alumina nanoplatelets. The flexural strength results indicated that the textured structure led to an improvement in the flexural strength, from 77 MPa to 124 MPa, despite the lower bulk density of the textured samples. This study demonstrates that commercially available binder jetting machines with the roller compaction feature can effectively produce textured ceramics with customized properties along desired directions.

Keywords

Binder jetting, Additive manufacturing, Roller compaction, Textured ceramics, Templated grain growth.

1 Introduction

Additive manufacturing has opened up new possibilities for the manufacturing industry, and binder jetting is one of the seven main categories of additive manufacturing techniques, as defined by ASTM [1]. The binder jetting process consists of two main steps: first, a layer of powder is formed, and second, a liquid binder is selectively jetted to join the powder particles in the already formed layer. This layer-by-layer printing process is repeated to produce a green part that is then subjected to debinding and sintering. Binder jetting offers several advantages over other additive manufacturing techniques, particularly in the manufacturing of ceramics [2–7]. For instance, a notable benefit is the absence of thermal residual stresses and thermal shock failure, which are common issues in the manufacturing of ceramics. In binder jetting, as the printing process takes place at room temperature and the post-processing under uniform heating conditions, these issues are avoided.

On the other hand, texturing has proved an effective approach to enhancing the structural and/or functional properties of ceramics, such the electrical conductivity, magnetic anisotropy, and electromechanical coupling coefficient of functional ceramics, and the fractural toughness of structural ceramics [8]. By preferentially aligning the grain during texturing, ceramics' characteristics could be tuned along a desired direction. Templated grain growth (TGG) is among the most widely used texturing methods [8]. TGG promotes grain growth along preferred orientations by incorporating templates into a matrix. In this method, grains with an anisometric shape, such as platelets, serve as the templates for subsequent epitaxial grain growth. During the fabrication of the green part, the templates are first uniformly dispersed and preferentially oriented across the matrix that usually consists of randomly oriented equiaxed grains. Eventually, the matrix grains are consumed by the epitaxial grain growth of the templates during sintering. Consequently, textured ceramics were achieved as a result of the growth of templates in their preferred orientations [8].

Aligning the templates in the preferred orientations is a crucial step in the TGG method. Techniques such as tape casting and extrusion have been used to align templates, but they are limited in their ability to create complex shapes [9–12]. On the other hand, additive manufacturing, which is renowned for fabricating complex shapes, also has the potential to align the template due to its intrinsic layer-by-layer process. Although a small number of studies showed the possibility

of texturing ceramics using additive manufacturing techniques such as vat photopolymerization and material extrusion [13–15], binder jetting is more preferable when it comes to the achievable part size and geometric flexibility (complimentary support for overhang structures). The authors recently reported a preliminary study that showed the possibility of texturing ceramics through press-compaction-assisted binder jetting with a lab-designed setup [16]. However, in that study, no binder was applied for simplicity. Furthermore, the press compaction feature is not commercially available yet. Therefore, it is still unknown whether binder jetting is capable of producing textured ceramics when binder is applied or when a commercially available machine is used. This study aims to fill this gap in the literature.

In this work, the green samples were fabricated using a commercially available binder jetting machine equipped with the roller compaction feature. Two types of powders were utilized: one with 100 wt.% alumina nanoparticles as the baseline, and the other with 75 wt.% alumina nanoparticles as the matrix and 25 wt.% alumina nanoplatelets as the templates for grain growth. This ratio of alumina nanoparticles to nanoplatelets was chosen based on the authors' previous study [16]. Density measurements, scanning electron microscopy (SEM) and X-ray diffraction (XRD) characterizations, and flexural tests were conducted on the resultant samples.

2 Materials and Methods

2.1 Powders

Two types of powders, without and with nanoplatelets, were prepared: one with 100 wt.% deagglomerated alumina nanoparticles (90–187125, Allied High Tech, USA), and the other with 75 wt.% deagglomerated alumina nanoparticles as the matrix and 25 wt.% alumina nanoplatelets (1344-28-1, Antaria Pty Ltd, Australia) as the templates. Figure 1 shows the morphology of the alumina nanoparticles and alumina nanoplatelets. As the sintering aids, calcium carbonate ($CaCO_3$) and silicon oxide (SiO_2) powders (US3701 and US1161M, US Research Nanomaterials, USA) with a 1:1 molar ratio were added to each type of alumina powder. The particle sizes of $CaCO_3$ and SiO_2 powders were smaller than 50 nm and 200 nm, respectively. The weight ratio of the sintering aids to the alumina powder is 1:20. Then the powders were mixed using a ball milling machine (Jar Rolling Mills, Paul O. Abbe, USA) with alumina balls for an hour at a milling speed of 160 RPM. To remove the large agglomerates, the powders were sieved using a 250 μm sieve after ball milling.

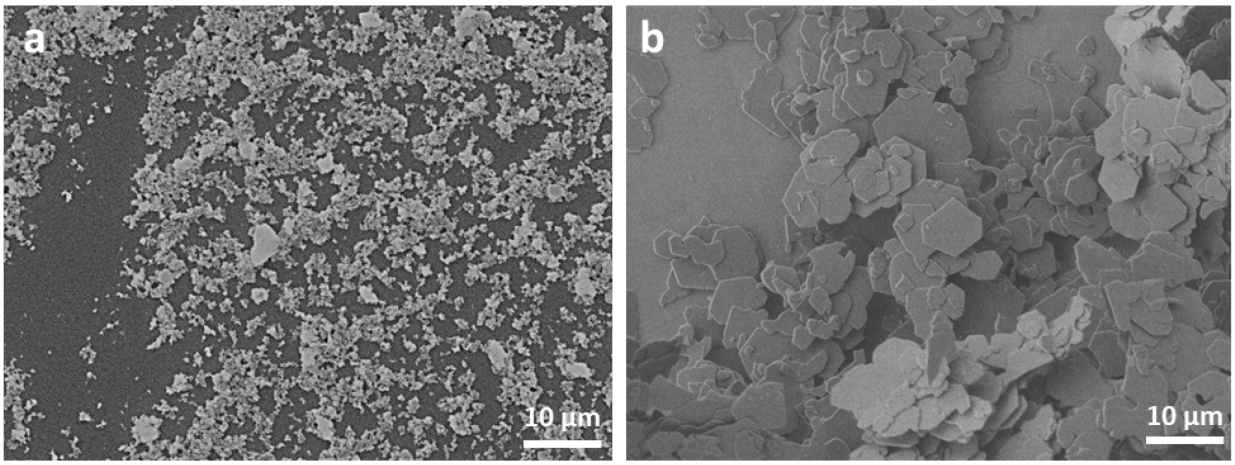

Figure 1. SEM images of a) alumina nanoparticles b) alumina nanoplatelets.

2.2 Roller-compaction-assisted binder jetting

The samples were printed using a binder jetting machine (Innovent+, ExOne company, USA) and an aqueous binder (BA005, ExOne company, USA). Detailed printing steps are outlined in a previous publication [17]. Figure 2 illustrates two key steps for aligning the nanoplatelets: the first step is dispensing and spreading (Figure 2a), and the second step is compaction (Figure 2b). During the dispensing and spreading step (Figure 2a), the powder is dispensed by ultrasonic vibration while the hopper moves over the build plate. Immediately after that, the roller with counter-rotating motion spreads the dispensed powder. The dispensed and spread powder filled the gap with a total thickness equal to layer thickness (25 µm) plus compaction thickness (200 µm). Then, in compaction (Figure 2b), the build plate ascends by compaction thickness (200 µm), and the roller compacts the spread powder from the total thickness (225 µm), i.e., layer thickness plus compaction thickness, to the final thickness (25 µm). Depending on the compaction pass number, this compaction step can be performed in multiple passes. The compaction pass number determines the number of back-and-forth passes required to apply compaction. In this work, the compaction pass number was set to 3, resulting in 3 back-and-forth passes (6 segments in total). Each segment involves raising the build plate by a fraction of compaction thickness (1/6 of 200 µm in this work) while the roller compacts the powder bed with a forward-rotating motion [18]. In addition, a difference between the actual and nominal roller diameters was employed to create a backward slip condition at the bottom of the roller and thus enhance the compaction effect. The

printing parameters used in this work were chosen based on the authors' previous studies and are summarized in Table 1 [17,19,20].

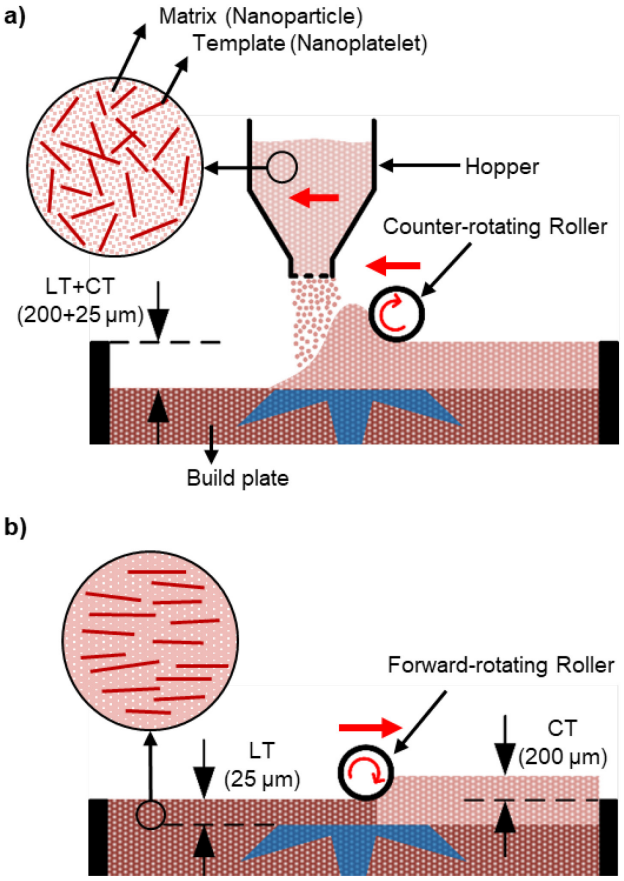

Figure 2. Schematic illustrations of a) dispensing and spreading, and b) compaction in the binder jetting machine equipped with the roller compaction feature (LT and CT mean layer thickness and compaction thickness, respectively).

Table 1. The printing parameters used in this work.

Printing parameter	***Value***
Layer thickness (µm)	25
Compaction thickness (µm)	200
Ultrasonic intensity (%)	100
Roller traverse speed during spreading (mm/s)	10
Roller rotation speed during spreading (rpm)	100
Roller traverse speed during compaction (mm/s)	3
Compaction pass number	3
Actual roller diameter (mm)	15
Nominal roller diameter (mm)	13.5
Binder saturation (%)	100
Binder set time (s)	5
Bed temperature (◦C)	50
Drying time (s)	10

2.3 Curing, depowdering, debinding, calcination, and sintering

After printing, the whole powder bed, which contains the printed samples and the loose powders, was transferred to an oven (DX402C, Yamato Scientific America, USA) for curing. It was performed at 200 °C for 5 hours to improve the strength of the printed samples. Following this step, the green samples were removed from the powder bed, and any remaining loose powders were cleaned from the green samples by a paint brush.

The next step involved placing the green samples in a furnace (KSL-1700X-A1-UL, MTI Corp., USA) for debinding, calcination, and full sintering following the heating profile demonstrated in Figure 3. The debinding step involved heating the samples at 480 °C for 2 hours to remove the cured binder. The calcination step involved heating the samples to 800 °C and keeping them at that temperature for 1 hour [21]. Finally, for full sintering, the temperature was raised to 1700 °C and held for 2 hours. The furnace was then turned off, and the samples were cooled down in the furnace until they reached room temperature. In addition, some samples were partially sintered: they were heated to 1500 °C instead of 1700 °C.

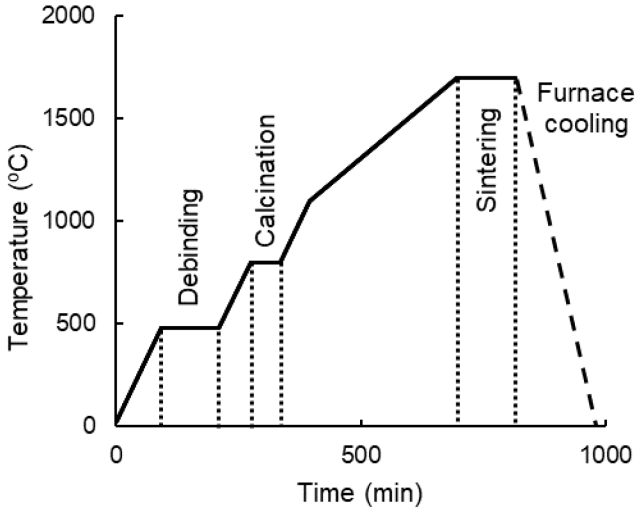

Figure 3. Heating profile used for debinding, calcination, and full sintering.

2.4 Density measurements

The bulk density of the fully sintered samples was measured using the Archimedes method [22]. The samples were boiled in water for 3 hours. Then the soaked and wet weights were measured using a density measurement kit (Density Determination Kit, Torbal, USA). Subsequently, the samples were dried in a furnace (KSL-1700X-A1-UL, MTI Corp., USA) at 150 ºC for 2 hours, and then the dry weight of the samples was measured. By knowing the dry, soaked, and wet weights of the samples, the Archimedes formulas were used to calculate the sintered density, apparent porosity, and closed porosity following the ISO 18754 standard [22]. The Archimedes method was described in detail in a previous publication [3].

2.5 Characterization of morphological and crystallographic textures

The morphological and crystallographic textures of the samples were assessed using SEM and XRD, respectively. To investigate the orientations of the templates, i.e., the nanoplatelets, partially and fully sintered samples were manually broken into two parts, and SEM images were taken on their facture surfaces. XRD was conducted on the side and top surfaces of the fully sintered sample with nanoplatelets to assess the textured structure. Additionally, XRD was performed on the top surface of the green and fully sintered samples with nanoplatelets and compared with the fully sintered sample without nanoplatelets to determine the effect of the grain growth during sintering on the textured structure. To quantify the degree of texture, the Lotgering

facture was determined. The detailed instructions for calculating the Lotgering factor are available in other work [8].

2.6 Flexural tests

To examine the effect of textured structure on the mechanical behavior of the fully sintered samples, two sets of flexural bars were prepared, one without nanoplatelets and the other with nanoplatelets. To achieve the dimensions of 25 × 3 × 2 mm^3, as specified in the ASTM-C1161 standard [23], the surfaces of the flexural bars were polished with SiC abrasive sandpapers with different grit grades of 80, 400, and 2000. A universal test machine (Insight 30, MTS, USA) equipped with a three-point fixture was used to carry out the flexural tests according to the parameters specified in the ASTM-C1161 standard [23]. To ensure statistical significance in the strength results, over 18 flexural bars were tested from each set. The strength distribution of each set was plotted using the Weibull statistic, and accordingly, its characteristic strength and Weibull modulus were calculated following the ASTM standard [24–26].

3 Results and discussion

3.1 Density and porosity

The bulk density, apparent porosity, and closed porosity of the fully sintered samples can be found in Figure 4. The bulk density results achieved in this work are comparable to the highest density values reported for binder jetting of alumina [17], which may be due to the addition of sintering aids to the powders and the strong roller compaction applied during the process. Comparing the samples without and with nanoplatelets indicates that adding the nanoplatelets led to a reduction in the bulk density and an increase in the apparent and closed porosities.

This reduction in the bulk density of the fully sintered samples with nanoplatelets can be attributed to the constraints from the nanoplatelets. Previous studies have shown that adding templates can hinder densification as the templates interfere with each other and limit grain growth [8,27,28]. Consequently, their results showed that the samples with templates exhibited lower sintered densities than those without them. Similarly, in this work, the lower sintered density of the samples with nanoplatelets can be related to their resultant constraints.

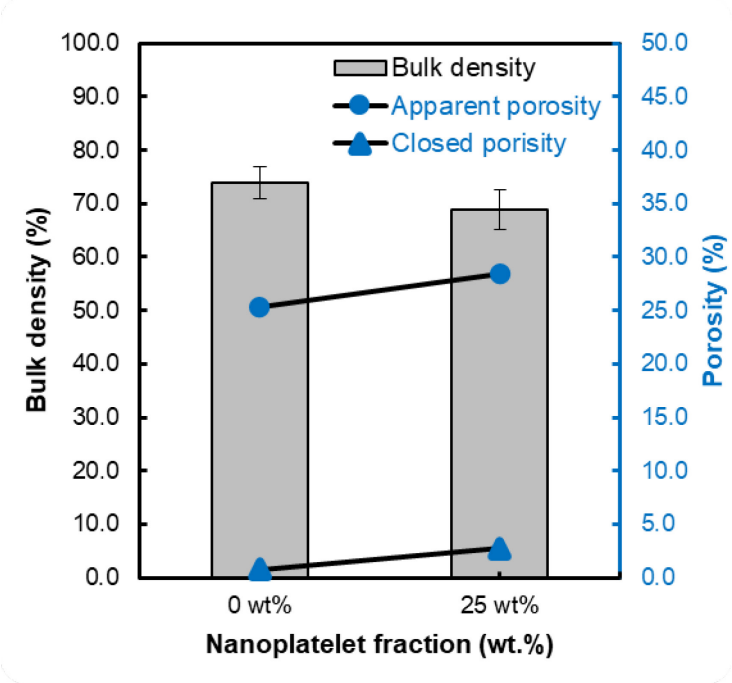

Figure 4. Bulk density, apparent porosity, and closed porosity of the fully sintered samples without and with nanoplatelets.

3.2 Morphological texture

Figure 5 shows the SEM images taken from the fracture surfaces of the fully sintered samples without and with nanoplatelets. In terms of pore distribution, the sample without nanoplatelets (Figure 5a) exhibits randomly distributed pores. However, the sample with nanoplatelets (Figure 5c) shows some degree of non-uniformity in the pore distribution, with some regions (bands) containing more densely packed grains and other regions (bands) having more pores. Furthermore, regarding the pore morphology, in the sample without nanoplatelets (Figures 5a and 5b), the grains and the pores are equiaxed without any specific shape. However, in the sample with nanoplatelets (Figures 5c and 5d), the grains and pores are horizontally elongated, i.e., perpendicular to the build direction. Closer examinations of SEM images with higher magnification (Figure 5d) reveal a clear and distinct morphological texture with mostly horizontal grain orientations.

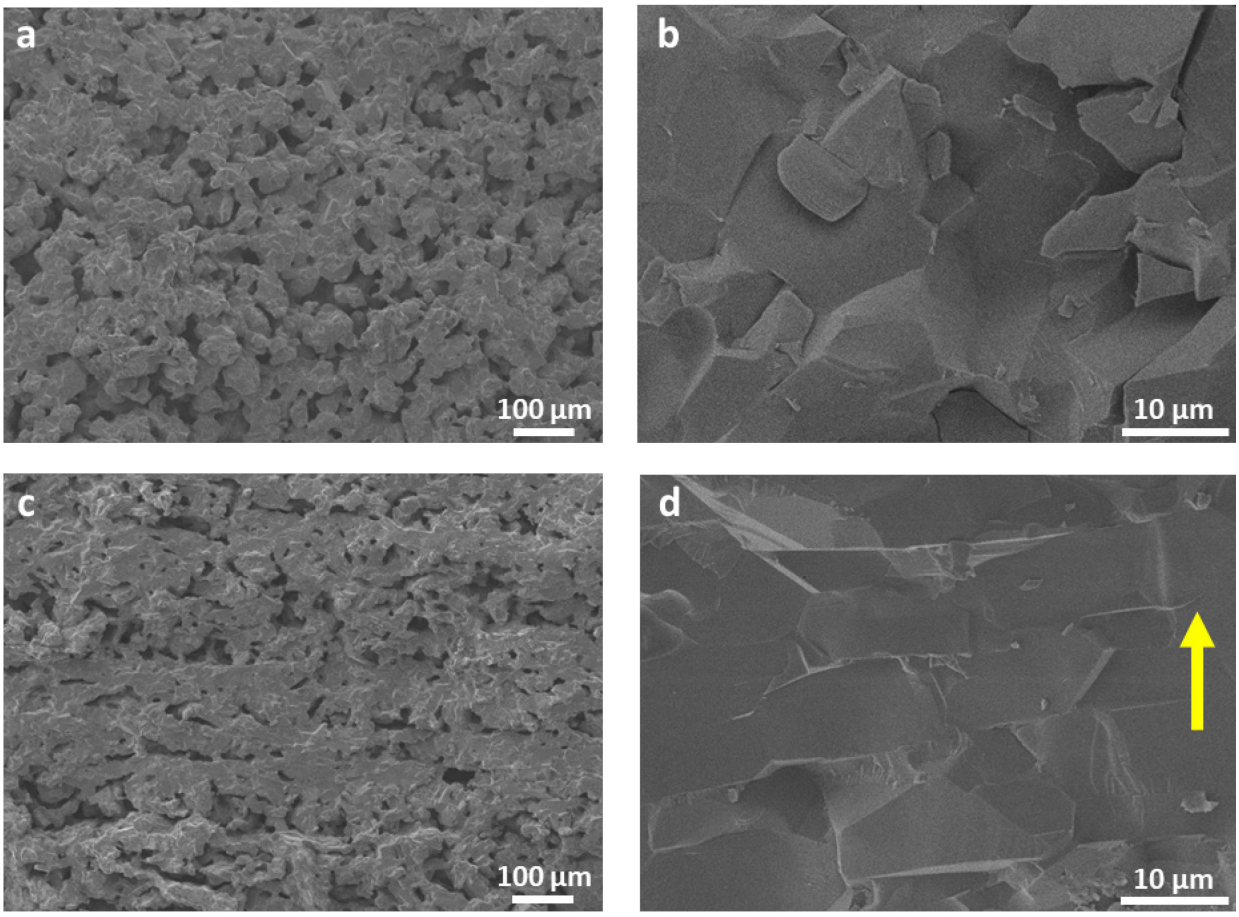

Figure 5. SEM images from the fully sintered samples a, b) without nanoplatelets and c, d) with nanoplatelets (the yellow arrow shows the build direction).

Figure 6 shows SEM images taken from the fracture surfaces of the partially sintered samples. The partial sintering allowed for easy detection of the orientations of nanoplatelets before the full growth. The results indicate that roller-compaction-assisted binder jetting was successful in achieving horizontal alignment of most of the nanoplatelets.

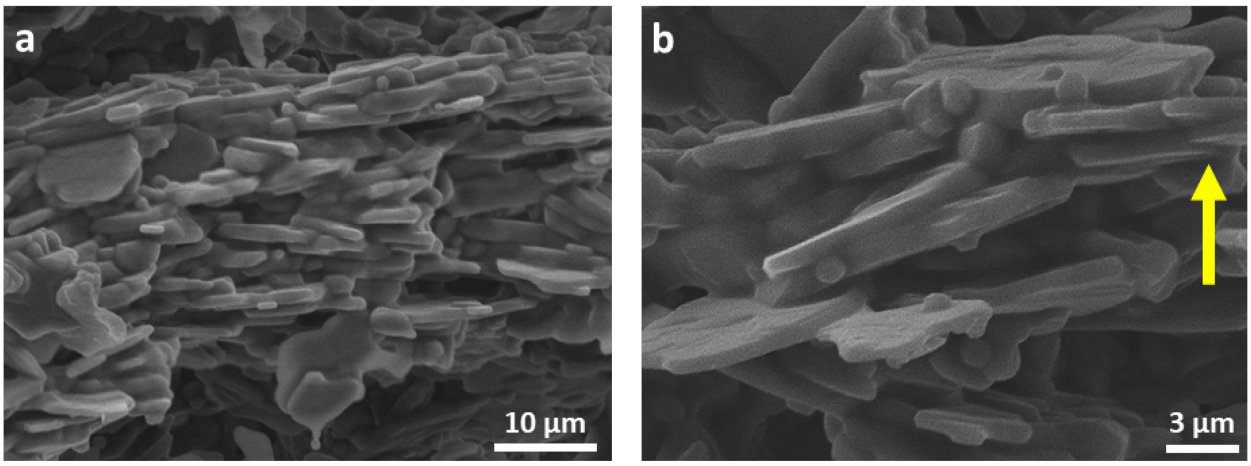

Figure 6. SEM images from the partially sintered sample with nanoplatelets with a) low and b) high magnifications (the yellow arrow shows the build direction).

3.3 Crystallographic texture

Figure 7 shows the XRD patterns of the side and top surfaces of the sintered sample with nanoplatelets. The side and top surfaces were parallel and perpendicular to the build direction, respectively. As demonstrated in Figure 7, it is evident that the intensities of the diffracted planes are drastically different when comparing side and top surfaces.

To explain the observed difference in peak intensities of the XRD patterns, the peaks were divided into three groups based on their relative orientations to the basal crystal plane of α-alumina, i.e., (0 0 L). A list of the values of these relative orientations (i.e., interplanar angles) is available in the literature [25]. Planes with relative orientations of less than 40 degrees were classified as small-tilt planes, while those with relative orientations of greater than 50 degrees were classified as large-tilt planes. The rest of the planes, i.e., those with relative orientations between 40 and 50, were classified as medium-tilt planes. These three groups, small, medium, and large-tilt planes, were color-coded in Figure 7 as red, orange, and blue, respectively.

Figure 7a shows that most of the high-intensity peaks on the side surface correspond to the large-tilt planes. In contrast, Figure 7b reveals that most of the high-intensity peaks on the top surface are associated with small-tilt planes. These distinct plane orientations observed between the side and top surfaces of the same sample provide clear evidence that the crystallographic texture has been achieved in the sample with nanoplatelets.

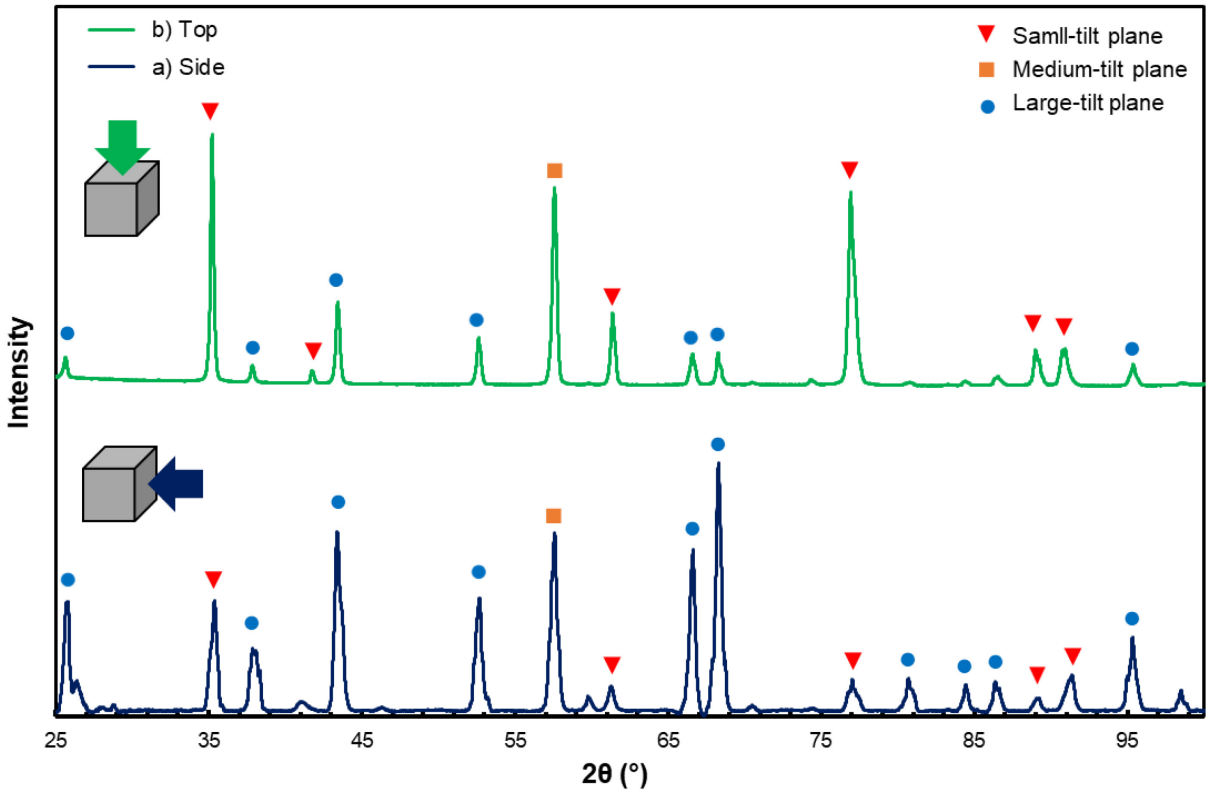

Figure 7. The XRD patterns of a) side and b) top surfaces of the fully sintered sample with nanoplatelets.

To trace the development of the textured structure during the TGG, the XRD pattern of the fully sintered sample without nanoplatelets (Figure 8a) was compared with those of the sample with nanoplatelets before and after full sintering (Figures 8b and 8c). The XRD pattern of the sample without nanoplatelets (Figure 8a) displays various peaks with a wide range of relative orientations to the basal crystal plane, such as high-intensity peaks of (1 0 4), (1 1 3), and (1 1 6), which are commonly identified as characteristic peaks of α-alumina [29,30]. The XRD pattern of the sample with nanoplatelets before sintering (Figure 8b) is quite similar to that of the sample without nanoplatelets after sintering (Figure 8a). However, after full sintering (Figure 8c), the intensities of the large-tilt planes decreased, such as (1 1 3), (0 2 4), (1 2 4), and (0 3 0), and on the other hand, the intensities of small-tilt planes increased, such as (1 0 4), (0 1 8), and (1 0 10). Figure 8c demonstrates the dominance of the small-tilt planes after full sintering.

The Lotgering factor was utilized in this work to quantify the degree of texture before and after full sintering, based on the XRD patterns [8]. Since the XRD results showed the templated

grain growth occurred in several small-tilt planes, these small-tilt planes of (0 0 6), (0 0 12), (1 0 10), (0 1 8), (0 2 10), and (1 0 4) with tilt angles of 0º, 0º, 17.5º, 21.5º, 32.2º, and 38.3º, respectively, were used as preferred lattice orientations to calculate the Lotgering factor [30]. The calculated Lotgering factors for the sample with nanoplatelets before and after full sintering were 0.04 and 0.43, respectively. These values confirm that while aligning the nanoplatelets is a crucial step in fabricating the textured structure, a significant amount of texture is developed during sintering and growth of the nanoplatelets.

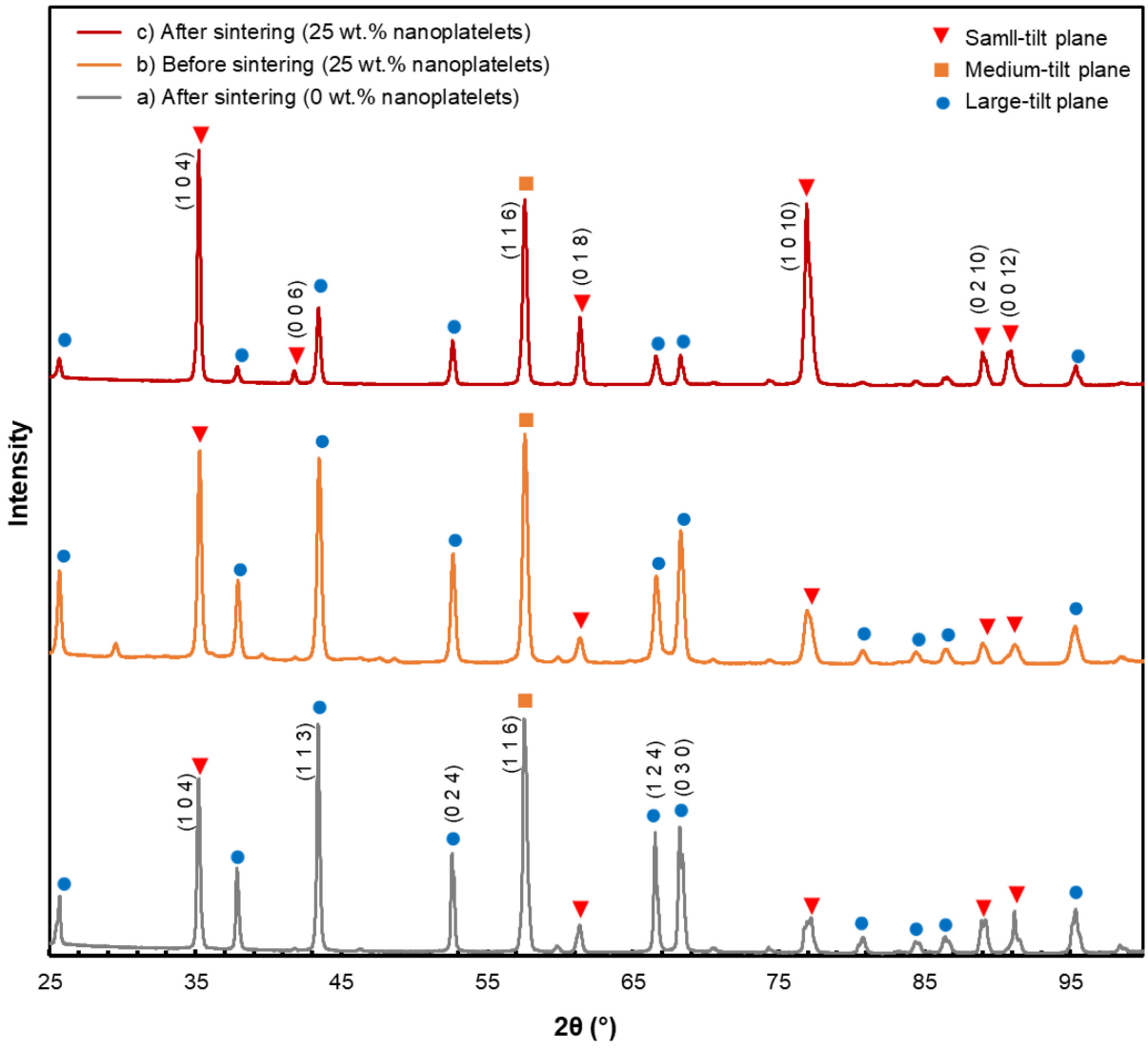

Figure 8. The XRD patterns of the top surface of a) the fully sintered sample without nanoplatelets, compared with the top surface of the sample with nanoplatelets b) before and c) after full sintering.

3.4 Flexural strength

The flexural strengths of the fully sintered samples, without and with nanoplatelets, were evaluated using Weibull statistics [24,25] and demonstrated in Figure 9 as the probability of failure versus flexural strength. To evaluate the effect of textured structure on the samples, the characteristic strengths, σ_0, and Weibull modulus, m, were evaluated for the samples without and with nanoplatelets according to the ASTM standard [26]. The results show that the addition of nanoplatelets and the achievement of textured structure resulted in a considerable improvement in the characteristic strength. The characteristic strength increased from 77 MPa to 124 MPa. The 90% confidence interval (CI) of the characteristic strength increased from [72-83 MPa] to [112-137MPa]. However, the Weibull modulus was slightly reduced from 5.2 to 3.9 with the addition of nanoplatelets and achievement of textured structure. The corresponding 90% CI of Weibull modulus changed from [3.9-7.0] to [2.9-5.2]. The reduction in Weibull modulus for the textured structure may be due to the lower bulk density and less uniform pore distribution. These factors can lead to more non-uniform failure and an increase in statistical variability in strength [31].

Despite a decrease in the sintered density of the samples, the flexural strength increased due to the achievement of the textured structure. The results suggest that texturing the structure through roller-compaction-assisted binder jetting could be used to enhance the mechanical strength.

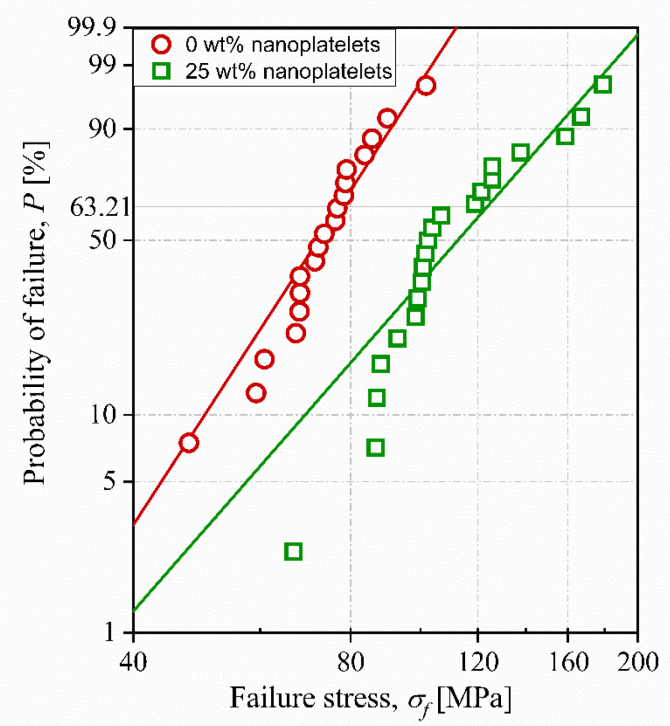

Figure 9. The flexural strength results for the fully sintered samples without and with nanoplatelets.

4 Conclusions

The addition of nanoplatelets resulted in a decrease in the bulk density, and an increase in open and closed porosities of the fully sintered samples. The SEM images of fracture surfaces showed that the nanoplatelets were aligned in the partially sintered sample, and the morphological texture was gained after full sintering. Furthermore, comparing the XRD patterns of the top and side surfaces of the sample with nanoplatelets indicated the achievement of the crystallographic texture. Analysis of the degree of texture through TGG steps demonstrated that texture was mostly developed during sintering and growth of nanoplatelets. Despite the lower bulk density, the textured sample showed a significantly higher flexural strength. These findings suggest that roller-compaction-assisted binder jetting can be utilized to enhance the mechanical strength of materials through texturing.

Data availability

The raw data and the processed data required to reproduce these findings are available upon request from the corresponding author.

Acknowledgement

This material is based upon work partially supported by the National Science Foundation under Grant No. 2401277.

Declaration of generative AI and AI-assisted technologies in the writing process

During the preparation of this work, the authors used ChatGPT in order to improve the readability. After using this tool/service, the authors reviewed and edited the content as needed and take full responsibility for the content of the publication.

References

[1] ASTM, Standard terminology for additive manufacturing – General principles – Terminology, ASTM Int. i (2015) 1–9. https://doi.org/10.1520/F2792-12A.2.

[2] A. Mostafaei, A.M. Elliott, J.E. Barnes, F. Li, W. Tan, C.L. Cramer, P. Nandwana, M. Chmielus, Binder jet 3D printing – process parameters, materials, properties, and challenges, Prog. Mater. Sci. (2020) 100684. https://doi.org/10.1016/j.pmatsci.2020.100684.

[3] W. Du, X. Ren, Z. Pei, C. Ma, Ceramic binder jetting additive manufacturing: A literature review on density, J. Manuf. Sci. Eng. 142 (2020) 1–66. https://doi.org/10.1115/1.4046248.

[4] J. Deckers, J. Vleugels, J.P. Kruth, Additive manufacturing of ceramics: A review, J. Ceram. Sci. Technol. 5 (2014) 245–260. https://doi.org/10.4416/JCST2014-00032.

[5] M. Moghadasi, W. Du, M. Li, Z. Pei, C. Ma, Ceramic binder jetting additive manufacturing: Effects of particle size on feedstock powder and final part properties, Ceram. Int. 46 (2020) 16966–16972. https://doi.org/10.1016/j.ceramint.2020.03.280.

[6] G. Miao, W. Du, M. Moghadasi, Z. Pei, C. Ma, Ceramic binder jetting additive manufacturing: Effects of granulation on properties of feedstock powder and printed and sintered parts, Addit. Manuf. 36 (2020) 101542. https://doi.org/10.1016/j.addma.2020.101542.

[7] M. Li, G. Miao, M. Moghadasi, Z. Pei, C. Ma, Ceramic binder jetting additive manufacturing: relationships among powder properties, feed region density, and powder

bed density, Ceram. Int. (2021). https://doi.org/10.1016/j.ceramint.2021.05.175.

[8] Z. Zhang, X. Duan, B. Qiu, Z. Yang, D. Cai, P. He, D. Jia, Y. Zhou, Preparation and anisotropic properties of textured structural ceramics: A review, J. Adv. Ceram. 8 (2019) 289–332. https://doi.org/10.1007/s40145-019-0325-5.

[9] F. Gao, R.Z. Hong, J.J. Liu, Y.H. Yao, C.S. Tian, Grain growth kinetics of textured 0.92Na0.5Bi 0.5TiO3-0.08BaTiO3 ceramics by tape casting with Bi2.5Na3.5Nb5O18 templates, J. Electroceramics. 24 (2010) 145–152. https://doi.org/10.1007/S10832-008-9549-4.

[10] M. Palizdar, C.M. Fancher, T.P. Comyn, T.J. Stevenson, S.F. Poterala, G.L. Messing, E. Suvaci, A.P. Kleppe, A.J. Jephcoat, A.J. Bell, Characterization of thick bismuth ferrite–lead titanate films processed by tape casting and templated grain growth, J. Eur. Ceram. Soc. 35 (2015) 4453–4458. https://doi.org/10.1016/J.JEURCERAMSOC.2015.08.037.

[11] Y. Kan, P. Wang, Y. Li, Y.B. Cheng, D. Yan, Fabrication of textured bismuth titanate by templated grain growth using aqueous tape casting, J. Eur. Ceram. Soc. 23 (2003) 2163–2169. https://doi.org/10.1016/S0955-2219(03)00035-9.

[12] T. Takeuchi, T. Tani, Y. Saito, Unidirectionally textured CaBi4Ti4O15 ceramics by the reactive templated grain growth with an extrusion, Japanese J. Appl. Physics, Part 1 Regul. Pap. Short Notes Rev. Pap. 39 (2000) 5577–5580. https://doi.org/10.1143/JJAP.39.5577/XML.

[13] A.K. Hofer, I. Kraleva, R. Bermejo, Additive manufacturing of highly textured alumina ceramics, Open Ceram. 5 (2021) 100085. https://doi.org/10.1016/j.oceram.2021.100085.

[14] R.L. Walton, E.R. Kupp, G.L. Messing, Additive manufacturing of textured ceramics: A review, J. Mater. Res. 36 (2021) 3591–3606. https://doi.org/10.1557/s43578-021-00283-6.

[15] R.L. Walton, M.J. Brova, B.H. Watson, E.R. Kupp, M.A. Fanton, R.J. Meyer, G.L. Messing, Direct writing of textured ceramics using anisotropic nozzles, J. Eur. Ceram. Soc. 41 (2021) 1945–1953. https://doi.org/10.1016/j.jeurceramsoc.2020.10.021.

[16] M. Moghadasi, A. Mahdaviarab, A.K. Hofer, R. Bermejo, Z. Pei, C. Ma, Press-compaction-assisted binder jetting of textured ceramics, Ceram. Int. (2023). https://doi.org/10.1016/J.CERAMINT.2023.09.265.

[17] M. Moghadasi, G. Miao, M. Li, Z. Pei, C. Ma, Combining powder bed compaction and nanopowders to improve density in ceramic binder jetting additive manufacturing, Ceram. Int. 47 (2021) 35348–35355. https://doi.org/10.1016/J.CERAMINT.2021.09.077.

[18] M. Li, X. Wei, Z. Pei, C. Ma, Binder jetting additive manufacturing: observations of compaction-induced powder bed surface defects, Manuf. Lett. 28 (2021) 50–53. https://doi.org/10.1016/j.mfglet.2021.04.003.

[19] G. Miao, M. Moghadasi, M. Li, Z. Pei, C. Ma, Binder Jetting Additive Manufacturing: Powder Packing in Shell Printing, J. Manuf. Mater. Process. 7 (2022) 4. https://doi.org/10.3390/JMMP7010004.

[20] G. Miao, M. Moghadasi, W. Du, Z. Pei, C. Ma, Experimental investigation on the effect of roller traverse and rotation speeds on ceramic binder jetting additive manufacturing, J. Manuf. Process. 79 (2022) 887–894. https://doi.org/10.1016/j.jmapro.2022.05.039.

[21] S. Baik, J.H. Moon, Effects of magnesium oxide on grain-boundary segregation of calcium during sintering of alumina, J. Am. Ceram. Soc. 74 (1991) 819–822. https://doi.org/10.1111/j.1151-2916.1991.tb06931.x.

[22] ISO, Fine ceramics (advanced ceramics, advanced technical ceramics) — determination of density and apparent porosity, ISO 18754. (2013). https://www.iso.org/standard/55448.html.

[23] ASTM, Standard test method for flexural strength of advanced ceramics at ambient, ASTM Int. (2002). https://doi.org/10.1520/C1161-18.1.

[24] W. Weibull, A statistical distribution function of wide applicability, J. Appl. Mech. 18 (1951) 293–297. https://doi.org/10.1115/1.4010337.

[25] W. Weibull, K.T. Högskolan, A statistical theory of the strength of materials, Fifteenthfirst Ed., Gen. Litografiska Anstalts Forl. (1939). http://www.worldcat.org/title/30416455.

[26] ASTM, Standard practice for reporting uniaxial strength data and estimating Weibull distribution parameters for advanced ceramics, ASTM Int. (2000) 1–17.

[27] R.J. Pavlacka, G.L. Messing, Processing and mechanical response of highly textured Al2O3, J. Eur. Ceram. Soc. 30 (2010) 2917–2925.

https://doi.org/10.1016/j.jeurceramsoc.2010.02.009.

[28] K. Takatori, H. Kadoura, H. Matsuo, S. Arakawa, T. Tani, Microstructural evolution of high purity alumina ceramics prepared by a templated grain growth method, J. Ceram. Soc. Japan. 124 (2016) 432–441. https://doi.org/10.2109/jcersj2.15261.

[29] T. Uchikoshi, T.S. Suzuki, H. Okuyama, Y. Sakka, Fabrication of textured alumina by electrophoretic deposition in a strong magnetic field, J. Mater. Sci. 39 (2004) 861–865. https://doi.org/10.1023/B:JMSC.0000012915.76707.CA.

[30] S. Honda, S. Hashimoto, S. Iwata, Y. Iwamoto, Anisotropic properties of highly textured porous alumina formed from platelets, Ceram. Int. 42 (2016) 1453–1458. https://doi.org/10.1016/j.ceramint.2015.09.090.

[31] Y. Fu, Z. Tao, X. Hou, Weibull distribution of the fracture strength of 99% alumina ceramic reshaped by cold isostatic pressing, Ceram. Int. 40 (2014) 7661–7667. https://doi.org/10.1016/j.ceramint.2013.12.053.